

Energy-efficient current-induced skyrmion phases in Co/Ni/Pt-based multilayers

Jeffrey A. Brock¹, Sergio A. Montoya², Mi-Young Im³, and Eric E. Fullerton¹

¹ Center for Memory and Recording Research, University of California San Diego, La Jolla, CA USA

² Naval Information Warfare Center – Pacific, San Diego, CA USA

³ Center for X-Ray Optics, Lawrence Berkeley National Laboratory, Berkeley, California, USA

Abstract:

We have studied the effects of electrical current pulses on skyrmion nucleation in a series of Pt/Co/Ni-based multilayers. Transmission X-ray microscopy reveals that by applying electrical current pulses of duration and current density on the order of $\tau=50\text{ }\mu\text{s}$ and $j=10^{9-10}\text{ A/m}^2$, respectively, in an applied magnetic field of $\mu_0 H_z=50\text{ mT}$, stripe-to-skyrmion transformations are attained. The skyrmions remain stable across a wide range of magnetic fields, including zero field. We primarily attribute the transition to current-induced Joule heating, with the minor contribution of spin-orbit torques. Reducing the magnetic moment and perpendicular anisotropy using rare-earth spacers lowers the current and magnetic field needed to accomplish the transition. These findings support the idea that energetic inputs allow for the formation and stabilization of skyrmions in a broader class of materials than previously thought possible, and that material properties can be tuned to yield a more energy-efficient stabilization of the skyrmion phase.

Introduction:

Over the past decade, there has been an increasing study of magnetic textures known as skyrmions because of their quantized spin topology.^{1,2,3} This spin structure gives rise to topologically enhanced stability and unique dynamics that are attractive for emerging data storage, memory, and computational applications.⁴ Creating a material system capable of hosting such a unique magnetic texture involves a delicate interplay between the exchange, dipolar, and anisotropy energies of the material. While it is possible to optimize these three energies alone to create a material capable of hosting skyrmions (as has been shown in Fe/Gd multilayers⁵), often an additional energetic contribution from the Dzyaloshinskii-Moriya interaction (DMI)^{6,7} is key to fostering skyrmions. In contrast to ferromagnetic exchange, the DMI favors a 90° canting of neighboring spins relative to one another.⁸ Initially, the skyrmion texture was first reported in a bulk crystal of the weak ferromagnet MnSi, where the presence of DMI was attributed to the material's non-centrosymmetric crystal structure.⁹ Over the ensuing years, the interfacial DMI due to symmetry breaking at a ferromagnet/heavy metal or oxide interface in structurally-asymmetric structures^{10,11,12,13,14} has been exploited to foster skyrmions in many multilayers (e.g., Refs 11, 15, 16, 17, 18, 19, 20, and references therein).

Recently, there has been interest in leveraging the effects of rapid heating to transform magnetic stripe domains into skyrmions.^{21,22,23,24} Micromagnetic and atomistic simulations have shown that a short timescale temperature rise in these systems can transition the sample between a variety of morphological magnetic domain phases, including the skyrmion state.²⁵ Crucially, experimental reports have demonstrated that skyrmions formed via Joule heating exhibit several attractive traits, such as stability against changes in the magnetic field (including at zero field), and even the ability to nucleate skyrmions in zero applied magnetic field (at $T > 380$ K) in some systems.²¹ However, there are still many open questions as to the physical nature of this thermally driven transition, including approaches by which the magnetic field and Joule heating necessary to drive the stripe-to-skyrmion transition can be reduced while still retaining the robust stability of the skyrmion phase.

We have chosen to study a multilayer of the base structure [Pt/Co/Ni]. Our choice of materials was motivated by reports suggesting that the Pt/Co and Pt/Ni interfaces can have different strengths of interfacial DMI, such that an additive DMI is obtained when they are

incorporated in structurally asymmetric materials stacks.²⁶ Additionally, Co/Ni-based systems have already been the subject of extensive study on account of the inherent tunability of their basic physical properties, such as the saturation magnetization, spin polarization, strength of perpendicular magnetic anisotropy, and Gilbert damping.^{27,28} Indeed, this ease with which the magnetic properties of Co/Ni-based systems can be adjusted has been capitalized to experimentally foster skyrmions in a variety of structures, including Pt/[Co/Ni]/Ir²⁹ and Pt/[Co/Ni/Co]/Au³⁰, albeit only stabilizing the skyrmion phase in an applied magnetic field.

Using resonant full-field magnetic transmission X-ray microscopy (MTMX) operating at the Co L_3 absorption edge (778 eV), we imaged the effects of applied magnetic fields and electrical current pulses on the magnetic domain morphology in several 10- μ m-wide, 3-mm-long [Co/Ni/Pt]-type patterned devices. It was found that current pulses that deliver a Joule heating on the order of 4 μ J in a 50 mT field were capable of completely transforming all stripes within the field of view of a [Co/Ni/Pt]₂₀ sample into skyrmions and that these skyrmions remained stable over an extended range of magnetic fields. By reducing the saturation magnetization and effective perpendicular anisotropy through the insertion of thin rare earth spacer layers within the ferromagnetic layers, the Joule heating needed to accomplish the same transition was reduced to \sim 0.05 μ J, while still retaining robust field stability. These results further support the idea that Joule heating in a magnetic field allows for the efficient nucleation of skyrmions in a broad class of multilayers and identifies pathways towards lowering the current density needed to achieve skyrmions by such means.

Results:

Figures 1(a-c) show MTXM images of the field-dependent magnetic domain morphology of a [Co/Ni/Pt]₂₀ patterned wire as a perpendicular magnetic field ($\mu_0 H_z$) was swept from negative saturation to positive saturation at room temperature. The contrast in these images reflects the perpendicular magnetization averaged over the thickness of the film, where opposite magnetization textures are represented as gray ($+M_z$) and black ($-M_z$) contrast. At remanence ($\mu_0 H_z = 0$ mT), the domain morphology primarily consists of disordered stripe domains with a width of $105 \text{ nm} \pm 12 \text{ nm}$ [Fig. 1(a)]. As the perpendicular field is increased ($\mu_0 H_z = +90, +250$ mT), the disordered stripe domains begin to contract [Fig. 1(b)] until only a few stripe textures are

observable in the field of view [Fig. 1(c)]. Throughout the field-induced evolution of the stripe domains, the [Co/Ni/Pt]₂₀ patterned wire does not exhibit a field-stabilized skyrmion state. Supplementary Fig. S1³¹ shows the field-dependent domain morphology in greater detail, obtained using a [Co/ Ni/ Pt]₂₀ continuous film.

Having established the [Co/Ni/Pt]₂₀ patterned wire does not form skyrmion phase in response to an applied magnetic field at room temperature, we proceeded to investigate the effects of applying electrical current pulses with different attributes (*e.g.*, electrical current density j , and pulse duration τ) on the field-dependent domain morphology. At any given field, the domain morphology was recorded before and after injecting a current pulse. After each trial, the domain morphology was reset by cycling the perpendicular field up to positive saturation, then reducing the field to negative saturation, and finally increasing field to the desired positive value (for further details, see the Methods section). Figures 1(d-f) show the domain morphology that was obtained after applying a single $\tau = 50$ μ s-long current pulse with density $j = 1.7 \times 10^{10}$ A/m² onto the domain states depicted in Figs. 1(a-c). In calculating j , we considered the current flowing uniformly across the thickness of the entire sample. At remanence ($\mu_0 H_z = 0$ mT), we find the electrical pulse primarily results in the local rearrangement of disordered stripe domains, without the formation of any new types of magnetic features [Figs. 1(a, d)]. Under moderate fields ($\mu_0 H_z = +90$ mT), the current excitation transforms a disordered stripe phase into a dense but disordered skyrmion phase [Figs. 1(b, e)]. Like most multilayered materials that host field-induced^{32,33} and current-induced³⁴ skyrmions, we observe that the individual features exhibit a shape that is not perfectly circular, resulting from pinning centers present throughout the film. The skyrmion features exhibit an average diameter of $69 \text{ nm} \pm 11 \text{ nm}$, which is comparable to the average stripe width of $66 \text{ nm} \pm 8 \text{ nm}$ before the application of the current pulse. Near magnetic saturation ($\mu_0 H_z = +250$ mT), we find the remaining disordered stripe domains are annihilated after applying the current pulse, with the patterned wire becoming uniformly magnetized in the direction of the applied field [Figs. 1(c, f)].

Next, the field-stability of the current-induced skyrmion phase in the [Co/Ni/Pt]₂₀ patterned wire was investigated as the magnetic field was reduced from the positive field at which skyrmions were nucleated by electrical currents towards negative saturation. Figure 2(a-c) shows the evolution of the current-induced skyrmion phase as the applied magnetic field was varied. As the field was reduced, the individual skyrmion features grow nonuniformly within their local vicinity

retaining their overall general shape; moreover, the skyrmion features do not elongate/recombine to form a disordered stripe phase, as commonly observed in multilayered materials hosting field-stabilized skyrmions. At remanence, the domain morphology consists of a close-packed skyrmion phase [Fig. 2(b)], which differs from the ground state that is obtained under perpendicular fields [Fig. 1(a)]. Reducing the magnetic field further ($\mu_0 H_z = -70$ mT), we observe that the close-packed skyrmion phase continues to persist [Fig. 2(c)].

Afterward, we explored in detail the current-induced morphological transformations that arise in the [Co/Ni/Pt]₂₀ patterned wire as a function of perpendicular field and current pulse width. Figure 3(a) shows the different degrees of stripe-to-skyrmion transformation that can be accessed under different $\tau - \mu_0 H_z$ combinations (including the behaviors noted in Fig. 1) when applying a single electrical pulse with fixed density $j = 1.7 \times 10^{10}$ A/m². Like before, the field was cycled after each trial. At remanence, we find that a single current pulse with durations varying from $\tau = 10$ μ s up to 100 μ s is unable to induce a stripe-to-skyrmion transformation (within our field of view). A similar observation is noted when applying a $\tau = 10$ μ s current pulse as a function of increasing field ($\mu_0 H_z = 0$ mT to +120 mT). Under moderate fields ($\mu_0 H_z = +50$ mT and +90 mT) we can access a $\tau - \mu_0 H_z$ phase region where the electrical pulse first transforms a disordered stripe phase into a coexisting stripe and skyrmion phase; then, as the current pulse width is increased, a high-density skyrmion phase is formed. In general, the density of the current-induced skyrmion phase appears to depend on the density of stripe domains present before the current pulse is applied (see Supp. Fig. S2). Under higher applied fields ($\mu_0 H_z = +120$ mT and +250 mT), two additional $\tau - \mu_0 H_z$ phase regions can be accessed - the current-induced contraction of stripe domains as well as a sparse stripe-to-sparse skyrmion transition. Near the saturation field ($\mu_0 H_z = +300$ mT), the application of electrical current pulses annihilated the low-density stripe domains. Overall, the phase diagram illustrates an array of magnetic phases that can be accessed using electrical pulses. The physical mechanisms involved in the current-induced stripe-to-skyrmion transformation will be discussed subsequently.

To explore the tuning of materials properties that facilitate efficient current-induced stripe-to-skyrmion transformation using electrical pulses with lower current density and lower perpendicular fields, we investigated an array of different multilayers with moderate DMI. In general, it has been shown that reducing the saturation magnetization (M_s) and effective perpendicular anisotropy (K_{eff}) can lower the energy barrier that separates the stripe and skyrmion

ground states in multilayered materials.^{35,36} One potential pathway to lowering these two properties is through the incorporation of a rare earth spacer layer between the Co and Ni, which is expected to couple antiferromagnetically with the Co and Ni to reduce M_S (through the creation of a net ferrimagnetic structure) while at the same time increasing the thickness of magnetic material in the structure and removing the Co/Ni interfaces, reducing K_{eff} .^{37,38,39,40} Static characterization indicates that the [Co/ Ni/ Pt]₂₀ sample exhibits M_S and K_{eff} values of 1010 kA/m and $5.1 \times 10^5 \text{ J/m}^3$, respectively (Supp. Fig. S3). In line with the previous discussion, incorporating a thin spacer layer of rare earth material in a sample of the form [Co/ Gd (0.4 nm)/ Ni/ Pt]₂₀ reduces M_S to 488 kA/m, while K_{eff} was roughly halved to $K_{\text{eff}} = 2.5 \times 10^5 \text{ J/m}^3$. The variation is considerably more dramatic when Tb was employed in a structure of the composition [Co/ Tb (0.4 nm)/ Ni/ Pt]₂₀, which exhibited $M_S = 512 \text{ kA/m}$ and $K_{\text{eff}} = 8.2 \times 10^4 \text{ J/m}^3$ – roughly an 80 % reduction in K_{eff} relative to the [Co/Ni/Pt]₂₀ sample. All samples exhibit the “sheared” perpendicular hysteresis loops characteristic of a multi-domain state at zero field (Supp. Fig. S3). The field-dependent domain morphology of [Co/Tb/Ni/Pt]₂₀ and [Co/Gd/Ni/Pt]₂₀ patterned wires reveal a field-driven skyrmion phase is not energetically accessible in these materials (Supp. Fig. S4). Similar to [Co/Ni/Pt]₂₀, both [Co/Tb/Ni/Pt]₂₀ and [Co/Gd/Ni/Pt]₂₀ exhibit disordered stripe phases at remanence, with stripes exhibiting an average width of $142 \text{ nm} \pm 18 \text{ nm}$ and $137 \text{ nm} \pm 13 \text{ nm}$ respectively. Given the reduction in M_S , we expected the stripe domain width to broaden based on magnetostatics.⁴¹

Figure 3(b) shows the current-induced morphological phases of a [Co/Tb/Ni/Pt]₂₀ patterned wire as a function of perpendicular field and current pulse-width. In general, comparable morphological phases are observed as in [Co/Ni/Pt]₂₀ [Fig. 3(a)] with two main distinctions: The diverse morphological phases can be accessed using a lower magnitude range of $\mu_0 H_z$ and a lower-magnitude current density pulse of $j = 2.4 \times 10^9 \text{ A/m}^2$ (i.e., one order of magnitude lower). Furthermore, the [Co/Tb/Ni/Pt]₂₀ sample exhibits a current-induced morphological phase that was unseen in [Pt/Co/Ni]₂₀ – the elongation of stripe domains in the direction of the electron flow (Supp. Fig. S5). Similar behavior has been previously observed in [Pt/CoFeB/MgO]₂₀, and it was attributed to a balance of ferromagnetic exchange, perpendicular anisotropy, and DMI energy in a high aspect ratio geometry of the narrow wire based on micromagnetic simulations.²¹

Discussion

While the phase diagram shown in Fig. 3 demonstrates a diversity of morphological phases can be accessed in [Pt/Co/Ni]-based multilayers, it says nothing as to the physical mechanism responsible for the transformation. Because our samples are seeded on and capped with materials that are known to exhibit opposite signed spin-Hall angles^{42,43}, a net spin-orbit torque (SOT) may be acting on the system. We have performed additional experiments in order to discern the effects of Joule heating and SOT, as proposed in Ref. 21. In the first set of tests, a composite pulse (consisting of a baseline and a spike component) was utilized to deliver the same net electron flow/SOT and Joule heating, while varying the maximum temperature attained by the sample. This was accomplished by modifying the relative delay of the spike pulse to the beginning, middle, and end of the baseline pulse [Fig. 4(a)]. The baseline pulse with no spike, of duration $\tau = 72 \mu\text{s}$ and current density $j = 2.5 \times 10^9 \text{ A/m}^2$, did not result in morphological transformations when applied on its own to a [Co/Tb/Co/Ni/Pt]₂₀ patterned wire under an applied field of $\mu_0 H_z = +173 \text{ mT}$ [Figs. 4(b, f)]. Like the other samples discussed thus far, this sample does not exhibit a field-stabilized skyrmion phase; the skyrmion phase is accessed by applying electrical current pulses within a $\tau - \mu_0 H_z$ window unique to the sample. The spike pulse had $\tau = 10 \mu\text{s}$ with current density $j = 5 \times 10^9 \text{ A/m}^2$ [Fig. 4(a)]. For a spike pulse applied at the beginning of the baseline pulse [blue pulse, Fig. 4(a)], the field-stabilized stripe phase rearranged slightly [Fig. 4(c, g)]. As the relative delay of the spike pulse was increased to the middle and end of the baseline pulse [green and red pulses, Fig. 4(a)], the number of current-induced skyrmions increases [Figs. 4(d, h) and Figs. 4(e, i), respectively]. These tests suggest the time-dependent thermal profile from Joule heating plays an important role in the current-induced stripe-to-skyrmion generation in [Co/Ni/Pt]-type samples. Specifically, as the delay of the spike pulse increases, so too does the maximum temperature reached by the sample – suggesting that temperature plays a strong role in promoting the observed morphological transformations. However, since it is known that Joule heating can enhance the effect of SOT acting on a ferromagnetic sample⁴⁴, this test does not allow for a complete disentanglement of the effects of Joule heating versus SOT.

In the second set of tests, the current density j and pulse width τ were varied in such a way that the Joule heating previously identified as necessary for a complete stripe-to-skyrmion transformation ($\sim 0.4 \mu\text{J}$) was supplied at differing timescales. Figure 5(a) schematically shows the different pulses that were injected to the [Co/Tb/Co/Ni/Pt]₂₀ patterned wire under an applied

field of $\mu_0 H_z = +173$ mT. A complete stripe-to-skyrmion transformation is observed using a 50 μ s-long pulse with current density $j = 5 \times 10^9$ A/m² [Figs. 5(b, e)]. As this pulse corresponds to the most rapid heating of the sample, it should lead to the largest increase in temperature before the heat dissipates. A similarly-complete stripe-to-skyrmion transformation occurs in response to a 200 μ s-long pulse with current density $j = 2.5 \times 10^9$ A/m² [Figs. 5(c, f)], implying that the maximum temperature (estimated temperature?) attained under these conditions is still enough to promote a complete morphological transition. However, when the Joule heating is supplied using an 800 μ s pulse of current density $j = 1.25 \times 10^9$ A/m² [Figs. 5(d,g)], significant dissipation is expected to occur during the heating process. Consequentially, the temperature attained by the sample is not high enough to promote the nucleation of skyrmions.

Additionally, we varied the capping layer composition of the [Co/Ni/Pt]-type samples from Ta to Pt to change the sign of the spin-Hall angle of the layer. It is expected that the use of a Pt capping layer should reduce the net SOT acting on the magnetic layers if a uniform Neel domain wall chirality is maintained through the thickness of the film. Alternatively, if the dipolar energy is sufficient to promote the formation of Neel caps^{5,45}, the use of a Pt capping layer would enhance the SOT. In Supp. Fig. S6, we demonstrate that there is an identical change in domain morphology in response to equivalent stimuli between samples with Ta and Pt capping layers – implying that the strength of SOT is not central to driving the stripe-to-skyrmion transformation in the [Co/Ni/Pt]-type samples.

To better understand the impacts of Joule heating on the stability of morphological phases in the [Co/Ni/Pt]₂₀ samples, we have applied the model of Ref. 36 to explore the size and stability of the isolated skyrmion bubble state formed in our samples. These calculations were performed using parameters extracted from the static characterization (save for the DMI energy density of 0.622 mJ/m², which was determined by measuring the in-plane field-induced domain expansion asymmetry⁴⁶ in thinner samples that reverse via large circular domains). In Supp. Fig. S7(a), the energy as a function of bubble diameter is shown for several $\mu_0 H_z$ proximal to the minimum $\mu_0 H_z = +50$ mT needed to elicit the skyrmion phase in the [Co/Ni/Pt]₂₀ sample. Besides predicting skyrmion diameters close to those experimentally observed, it is apparent that increasing the field even by 10-mT increments can substantially shallow the energy barriers separating different morphological states. Similar calculations for the [Co/Tb/Ni/Pt]₂₀ sample [Supp. Fig. S7(b)] illustrates that the reduced M_S and K_{eff} of this sample leads to shallower energy barriers between

morphological states. Nonetheless, for all fields and samples considered, quasi-static variations in $\mu_0 H_z$ or temperature would likely be insufficient to overcome the well.²³

Although Joule heating appears to be the strongest actor in driving the observed morphological transformations, there are some peculiarities to our results that cannot be explicitly attributed to Joule heating. Take, for example, the three trials indicated by the dashed red box on the left-hand side of Fig. 3(a), over which the current pulse width τ varies only by 10 μs . Figure 5 shows the domain morphology before [Figs. 5(a-c)] and after [Figs. 5(d-e)] these three current pulses, with minute variation of τ and fixed current density, were applied on the domain states formed under $\mu_0 H_z = +50$ mT. We observe that the $\tau = 50$ μs current pulse [Figs. 5(a, d)] results in a rearrangement of magnetic stripe domains across the whole field of view. For a $\tau = 55$ μs pulse, we again primarily observe the reorganization of stripe domains, with sporadic stripe-to-skyrmion transformations [Figs. 5(b, e)]. In contrast, a $\tau = 60$ μs pulse, completely transforms the stripe phase into a closed-packed skyrmion lattice phase [Figs. 5(c, f)]. To rule out cumulative heating from applying a sequence of pulses in rapid succession, the sample sat idle for several minutes between measurements. It can reasonably be presumed that the variation in maximum temperature induced by these three pulses of such a similar duration cannot be significant. Based on the models presented in Supp. Fig. S8(a), such small differences in temperature should not dramatically shallow the energy separation between the stripe and skyrmion phases; this suggests that other physical mechanisms (namely, SOT) play a role in the current-induced stripe-to-skyrmion nucleation.

To glean a picture of how the ease of skyrmion nucleation via Joule heating varies between the samples discussed above, we consider two parameters: The Joule heating necessary to induce the transition ($\Delta E_{\text{st} \rightarrow \text{sk}}$), and the magnetic field in which the pulse is applied ($\mu_0 H_z_{\text{st} \rightarrow \text{sk}}$). To simplify comparisons, we consider the pulse of minimum τ and j needed to drive a complete stripe-to-skyrmion transition in the lowest $\mu_0 H_z$ possible for a given sample at room temperature (for additional information, see Methods). In Fig. 6(a), a comparison of $\Delta E_{\text{st} \rightarrow \text{sk}}$ for our samples, and for other systems in which skyrmion nucleation via Joule heating was studied are shown. The data for the [Pt/Co/Ni]₃₀ and [Pt/Co/Ni]₂₀ samples indicates that one way to reduce the heating needed to drive a complete stripe-to-skyrmion transition is by reducing the total thickness of the sample by a third, which lowers $\Delta E_{\text{st} \rightarrow \text{sk}}$ by nearly one order of magnitude. However, reducing M_s and K_{eff} has a more dramatic effect, lowering $\Delta E_{\text{st} \rightarrow \text{sk}}$ by more than two orders of magnitude in

[Co/Tb/Ni/Pt]₂₀ relative to [Co/Ni/Pt]₂₀. In comparison to other systems in which skyrmion nucleation in multilayers has been attributed to Joule heating^{21,22}, the systems containing rare earth spacers allow for a complete stripe-to-skyrmion transition via a comparable amount of Joule heating. The plot of $\mu_0 H_{z \text{ st} \rightarrow \text{sk}}$ for different sample compositions [Fig. 6(b)] shows a similar correlation to the thickness, M_s , and K_{eff} of the samples.

Conclusion

We have systematically studied the effect of electrical current pulses on the nucleation and stabilization of skyrmions in a variety of [Pt/Co/Ni]-based multilayers. A series of tests indicates that Joule heating is primarily responsible for the transformations in domain morphology observed, but that other mechanisms (*e.g.*, spin-orbit torques) play an assisting role. Furthermore, we have shown that lowering the saturation magnetization and effective perpendicular magnetic anisotropy dramatically reduces the current density and magnetic field necessary to drive a complete stripe-to-skyrmion transition, while still retaining attractive magnetic properties, such as zero-field skyrmion stability. Besides illustrating pathways towards reducing the energetic input necessary to nucleate skyrmions, these results further support the idea that Joule heating can enable the stabilization of skyrmions in a broad class of materials, over a wide range of environmental conditions, and in systems that do not require such a precise balance in energy contributions to be attained during the deposition process. Our results provide a pathway to tailor material properties to achieve energy-efficient current-induced skyrmion phases in multilayers.

Experimental Details:

Sample Fabrication and Static Characterization

Using DC magnetron sputtering, samples of the composition (from the substrate to top layer) Ta (2 nm)/Pt (5 nm)/[Co (0.7 nm)/Ni (0.5 nm)/Pt (0.7nm)]₂₀/Ta (5 nm) were deposited at room temperature using an Argon process gas pressure of 3 mTorr in a chamber whose base pressure was less than 1×10^{-8} Torr. For magnetic characterization, samples were grown on Si substrates with a 300-nm-thick thermal oxide coating. For full-field soft X-ray transmission microscopy experiments, samples were grown on 100-nm-thick SiN₃ membrane windows. Samples intended for electrical current studies were patterned into 10- μm -wide, 3-mm-long wires

using metal lift-off ultra-violet photolithography. Magnetometry measurements were performed at room temperature in both the out-of-plane and in-plane geometries using vibrating sample magnetometry (VSM) to determine the saturation magnetization (M_S) and effective perpendicular magnetic anisotropy (K_{eff}) from the saturation of the in-plane hard axis loop. In calculating volumetric parameters from the VSM data, only the thickness of the magnetic layers was considered.

Imaging

The evolution of the magnetic domain morphology as a function of the out-of-plane field and in response to electrical current pulses was assessed using resonant full-field magnetic transmission X-ray microscopy (MTXM) at Beamline 6.1.2 of the Advanced Light Source at Lawrence Berkeley National Laboratory.⁴⁷ Due to the non-uniformity of the illuminating spot projected on the sample, only representative areas of the entire micrograph collected are shown in the figures. All MTXM data was collected using circularly polarized X-rays resonant to the Co L_3 adsorption edge (778 eV).

Application of Electrical Current Pulses

Electrical current pulses were applied using an Agilent Technologies 81150A Pulse Function Arbitrary Generator. For all current densities and pulse durations discussed in this study, the leading/trailing edges of the pulse were set to 6 ns. Before each new trial, the magnetization of the sample was saturated in a positive field, followed by saturation in a negative field, followed by stabilization at the target positive field. The desired characteristics of the applied current pulses were verified using an oscilloscope connected at the ground end of the circuit. The electrical resistance of the samples was monitored throughout the experiments to ensure that the electrical current pulses did not appreciably alter the material properties. The pulse energy was calculated from the sample resistance, and the duration and voltage of the electrical pulse supplied. The minimum amount of Joule heating necessary to induce the stripe-to-skyrmion transition was determined as follows: First, the applied field was set to the point at which the hysteretic region of the magnetization curve for the sample in question first begins to open up when sweeping the field towards positive saturation. Next, the current pulse duration was fixed to 50 μs while applying electrical pulses of gradually increasing magnitude until a complete stripe-to-skyrmion transition

was observed. From this point, the pulse duration and applied magnetic fields were systematically varied to explore the responses. To avoid damaging the samples, we did not increase the pulse energy above the threshold Joule heating identified.

Acknowledgements

Imaging work at the ALS was supported by the U.S. Department of Energy (DE-AC02-05CH11231). J.A.B. and E.E.F. acknowledge support for sample fabrication, modeling, testing and synchrotron measurements by Quantum-Materials for Energy Efficient Neuromorphic Computing, an Energy Frontier Research Center funded by DOE, Office of Science, BES under Award No. DE-SC0019273.. M.-Y.I. acknowledges support by Lawrence Berkeley National Laboratory through the Laboratory Directed Research and Development (LDRD) Program and by the National Research Foundation of Korea (NRF) grant funded by the Korea government (MSIT)(NRF-2019R1A2C2002996, NRF-2016M3D1A1027831, and NRF-2019K1A3A7A09033400). This work was performed in part at the San Diego Nanotechnology Infrastructure (SDNI) of UCSD, a member of the National Nanotechnology Coordinated Infrastructure, which is supported by the National Science Foundation (ECCS-1542148).

Author Contributions

E.E.F., J.A.B., and S.A.M. conceived and designed the experiment. J.A.B. fabricated the samples used in the experiment. J.A.B., S.A.M., and M.Y.I. performed the imaging of the samples. J.A.B. wrote the manuscript. E.E.F. oversaw the entire project. All authors contributed to and commented on the manuscript.

Competing Financial Interests

The authors declare no competing interests.

Main text figures:

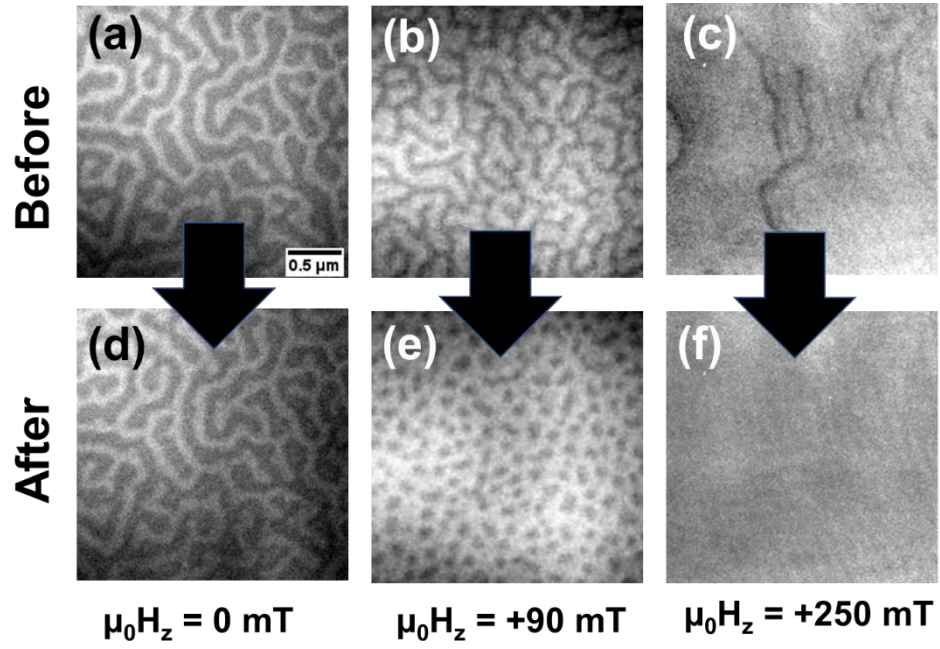


Figure 1. MTXM images illustrating the effect of a 60- μs -long current pulse of density $1.7 \times 10^{10} \text{ A/m}^2$ on the domain morphology of a $[\text{Co/Ni/Pt}]_{20}$ wire for $\mu_0 H_z = 0$ (a, d), +50 (b, e), and +250 mT (c, f) before and after the current is applied. The indicated perpendicular field $\mu_0 H_z$ was maintained before, during, and after the current pulse was applied. Low-contrast vertical lines observed in the foreground of (c, f) are artifacts of the MTXM optics.

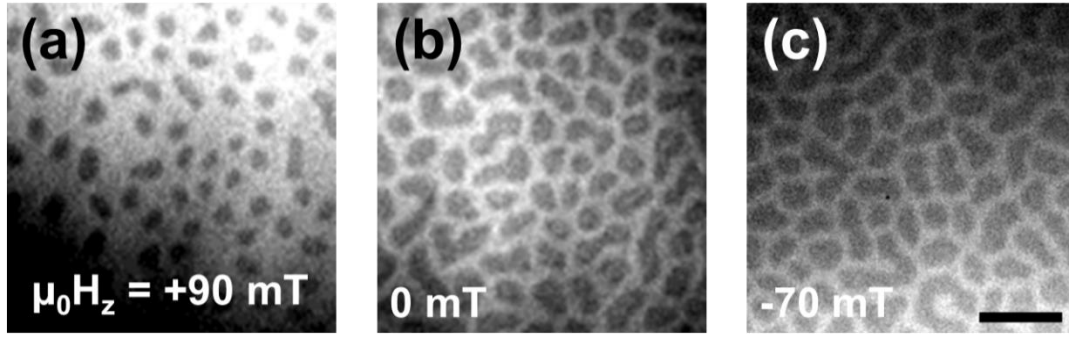


Figure 2. MTXM images of the skyrmion phase in the [Co/ Ni/ Pt]₂₀ sample as the out-of-plane field strength was varied. Before imaging, the stripe-to-skyrmion transformation was accomplished by applying a 60- μ s current pulse of density 1.7×10^{10} A/m² in a field of $\mu_0 H_z = +190$ mT. (bar = 500 nm)

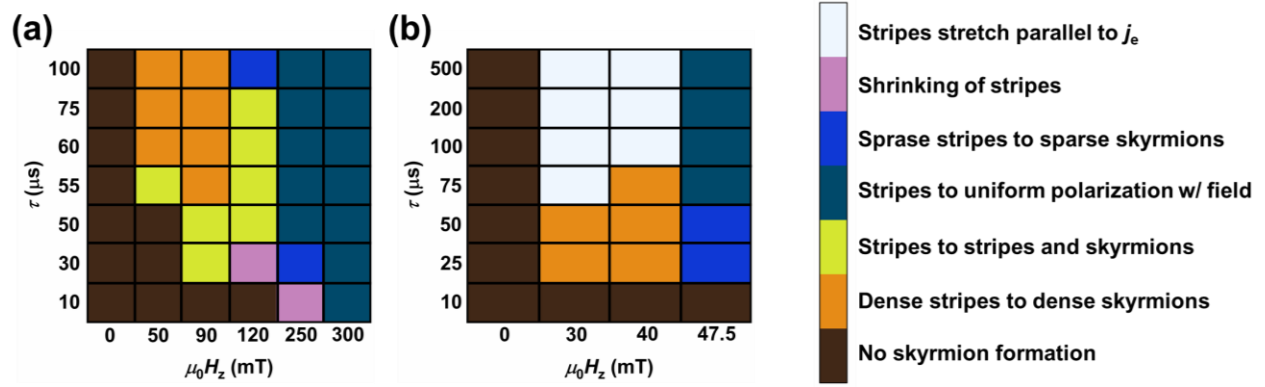
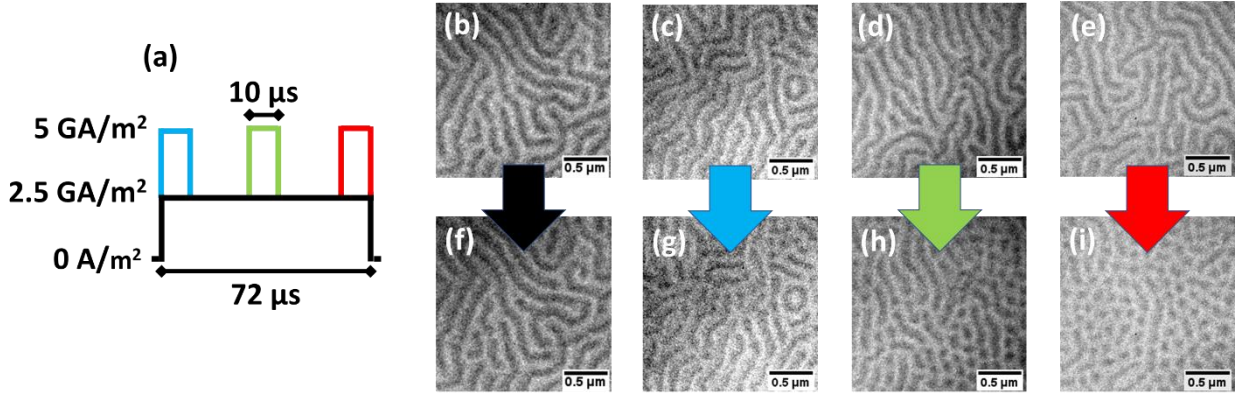


Figure 3. τ - $\mu_0 H_z$ phase maps for the (a) [Co/ Ni/ Pt]₂₀ and (b) [Co/ Tb/ Ni/ Pt]₂₀ samples indicating the change in morphology observed after pulses of $j = 1.7 \times 10^{10} \text{ A/m}^2$ and $j = 2.4 \times 10^9 \text{ A/m}^2$ (respective to each sample) were applied for various durations (τ) and out-of-plane magnetic field strengths ($\mu_0 H_z$). Before each measurement, the magnetic field was swept to both positive and negative saturation before setting the target magnetic field strength for the trial. Note that both the τ and $\mu_0 H_z$ -axes are not linearly scaled.



11

Figure 4. (a) Depiction of the composite pulse employed to delineate between Joule heating and spin-orbit torques. (b-i) MTXM images of a [Co/Tb/Co/Ni/Pt]-type sample illustrating the effects delivering the same Joule heating and same net electron flow by changing the relative delay of the spike pulse to the (c, g) beginning, (d, h) middle, and (e, i) end of the baseline pulse in a field of $\mu_0 H_z = +173$ mT. (b, f) demonstrates the effect of only applying the baseline pulse.

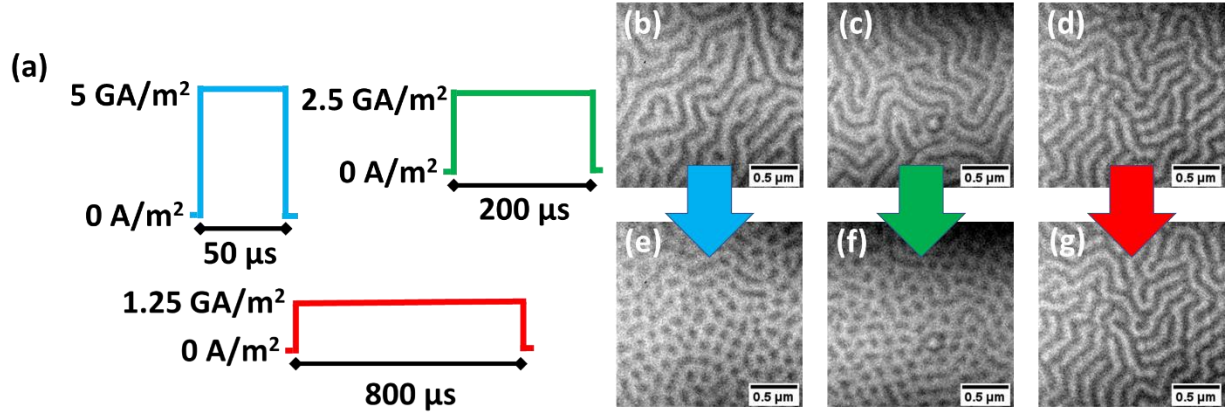


Figure 5. (a) Schematic depictions of the variation in pulse duration τ and current density j used to examine the impact of supplying an equivalent Joule heating ($\sim 0.4 \mu\text{J}$) using 50 μs (blue), 200 μs (green), and 800 μs (red)-long pulses. (b-g) MTXM images of a [Co/ Tb/ Co/ Ni/ Pt]-type sample illustrating the effect of delivering the 50 μs (b,e), 200 μs (c,f), and 800 μs (d,g)-long pulses illustrated in (a) in a perpendicular field of $\mu_0 H_z = +173 \text{ mT}$.

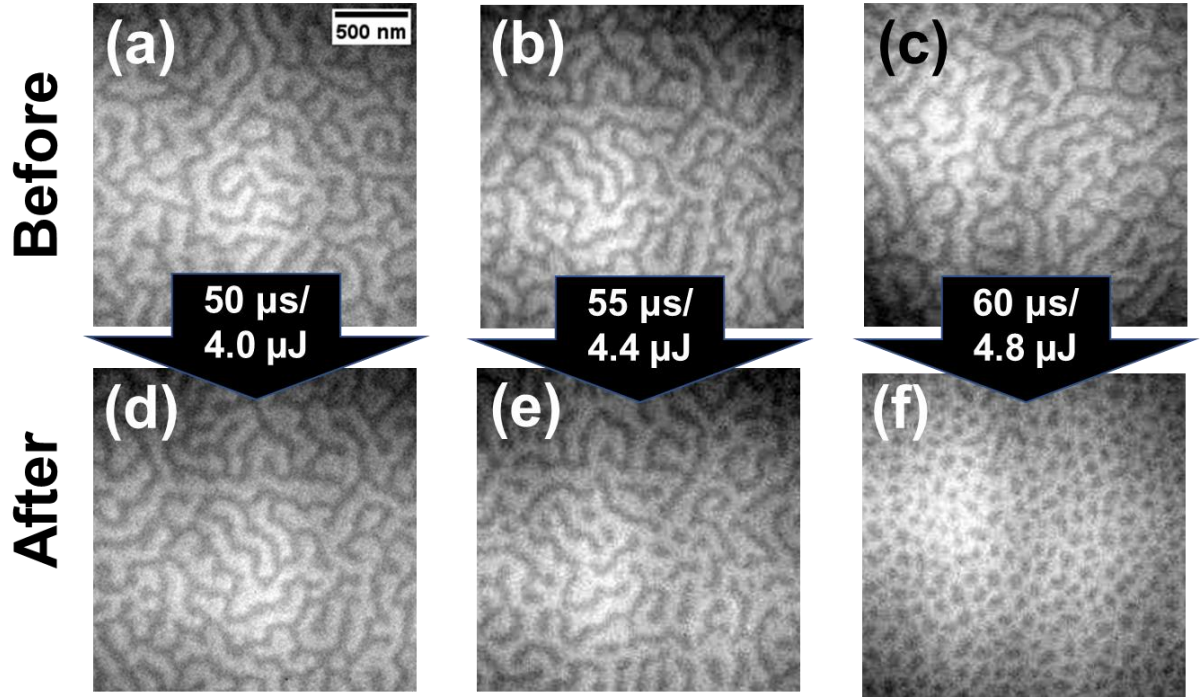


Figure 5. MTXM images before (a-c) and after (d-f) an electrical current pulse of varying duration was applied to a $[\text{Co/Ni/Pt}]_{20}$ sample. In all cases, the current pulse density was $j = 1.7 \times 10^{10} \text{ A/m}^2$ and $\mu_0 H_z = +90 \text{ mT}$. The Joule heating corresponding to each pulse duration is also indicated.

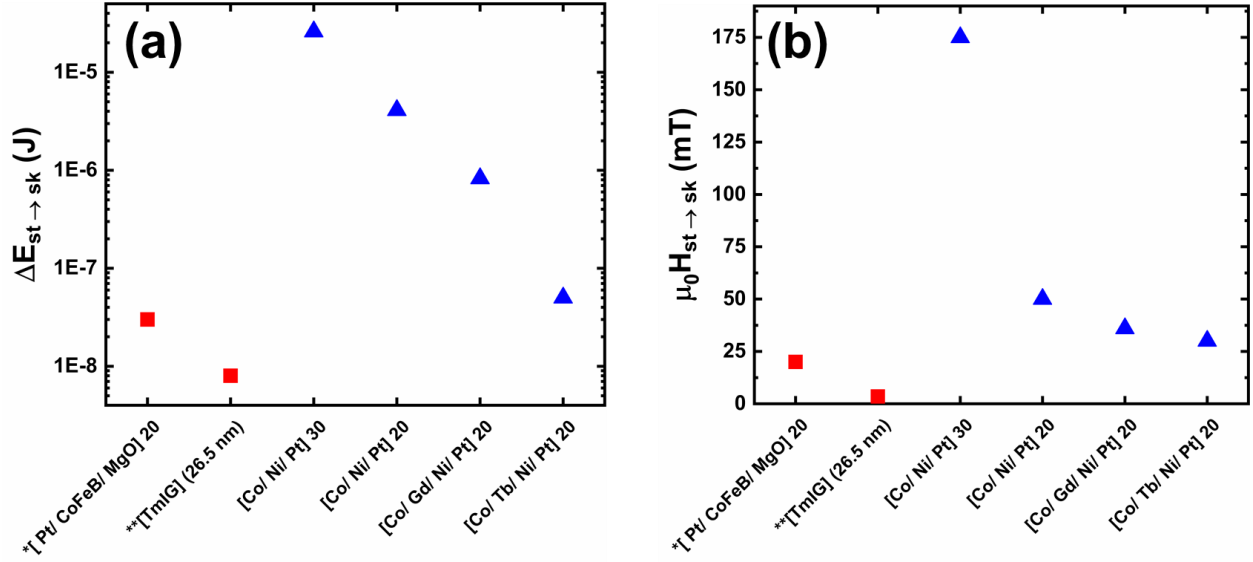
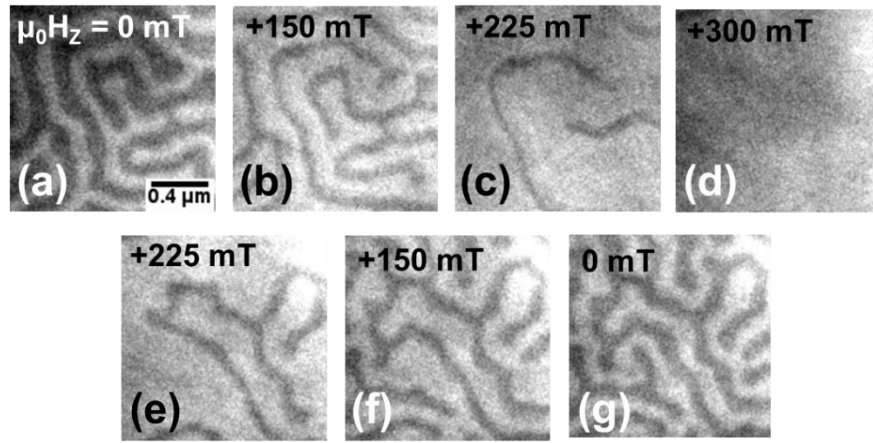
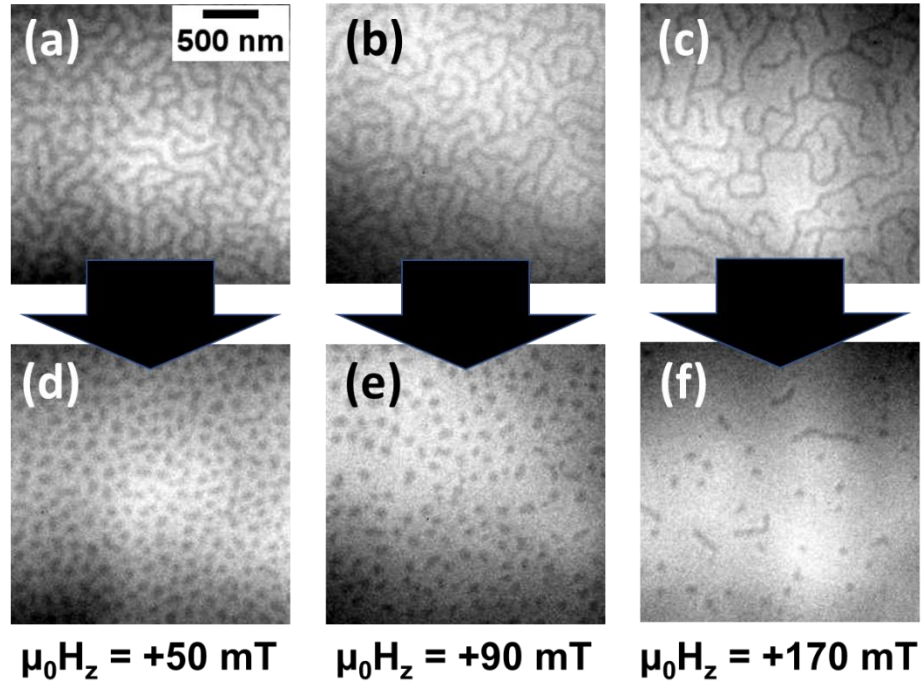


Figure 6. (a) The Joule heating ($\Delta E_{st \rightarrow sk}$) and (b) perpendicular field ($\mu_0 H_{st \rightarrow sk}$) necessary to initiate a complete stripe-to-skyrmion transition in the [Pt/Co/Ni]-based samples reported here (blue triangles) and in three other previously-reported systems in which the effects of Joule heating were investigated (red squares). Data corresponds to the necessary Joule heating at the lowest possible (or reported^{21,23}) magnetic field.

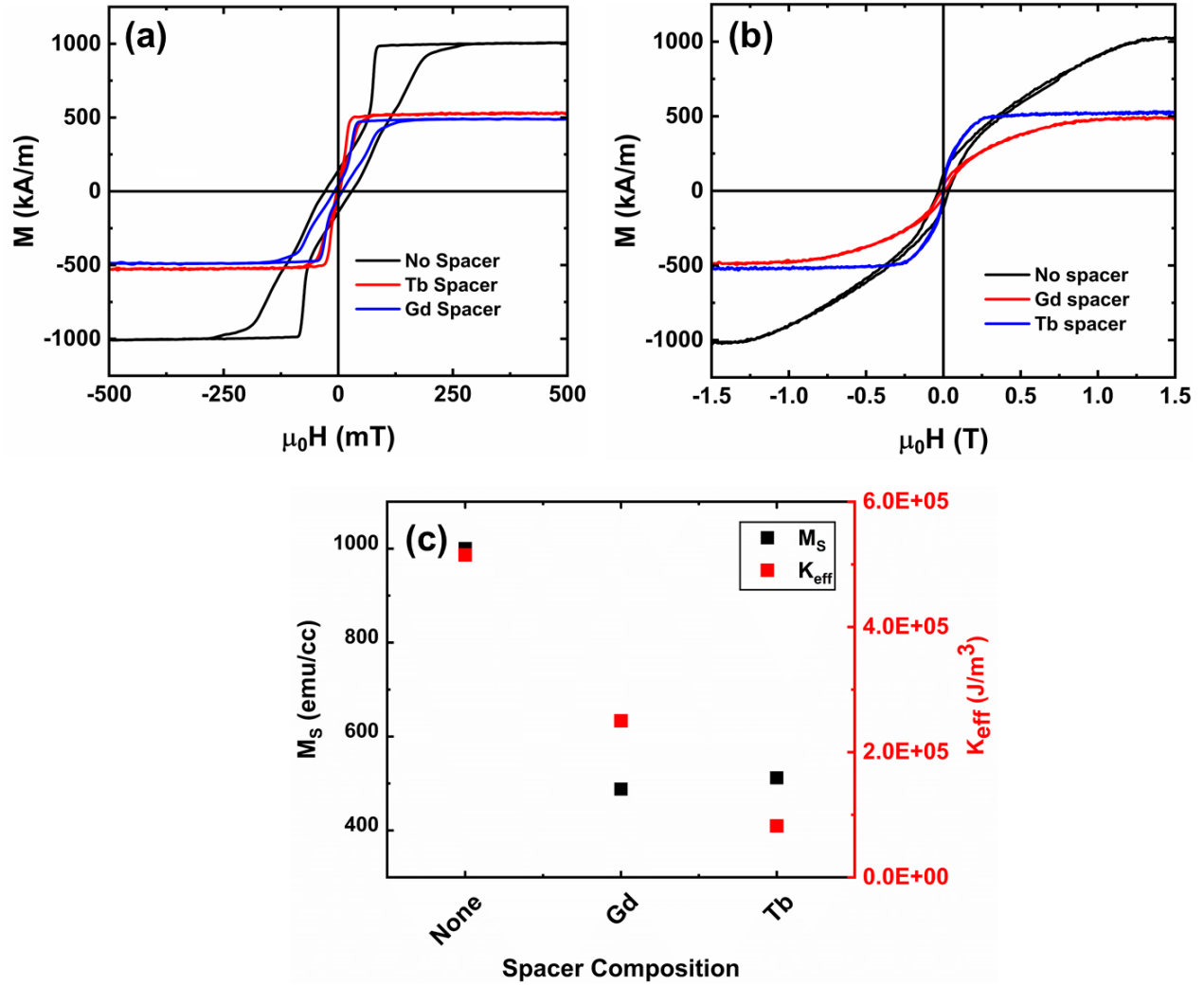
Supplemental Figures:



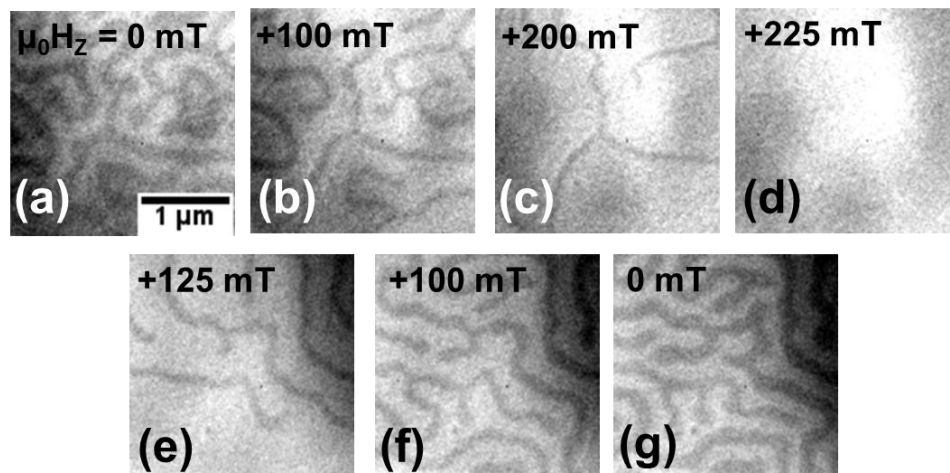
Supplemental Figure S1. Magnetic transmission X-ray microscopy (MTXM) images of the magnetic domain morphology as an out-of-plane magnetic field ($\mu_0 H_z$) was swept from zero towards positive saturation then back to zero in a Ta (2)/Pt (5)/[Co (0.7)/ Ni (0.5)/Pt (0.7)]₂₀/Ta (5) (thicknesses in nm) sample.



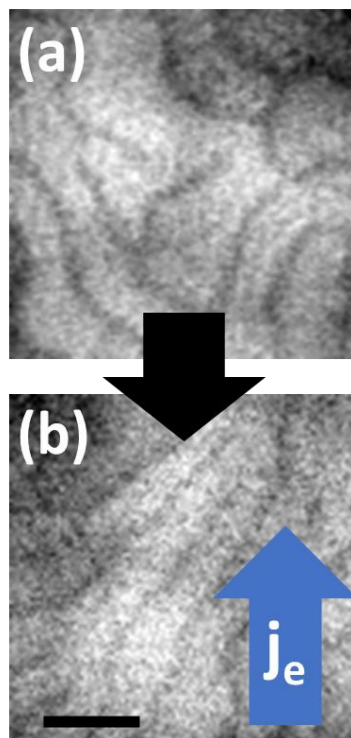
Supplemental Figure S2: MTXM images illustrating the effect of applying a $\tau = 100 \mu\text{s}$ -long current pulse with density $1.7 \times 10^{10} \text{ A/m}^2$ on the domain morphology of Ta (2)/Pt (5)/[Co (0.7)/Ni (0.5)/Pt (0.7)]₂₀/Ta (5) (thicknesses in nm) wire for applied magnetic fields of $\mu_0 H_z = +50$ (a, d), +90 (b, e), and +120 mT (c, f).



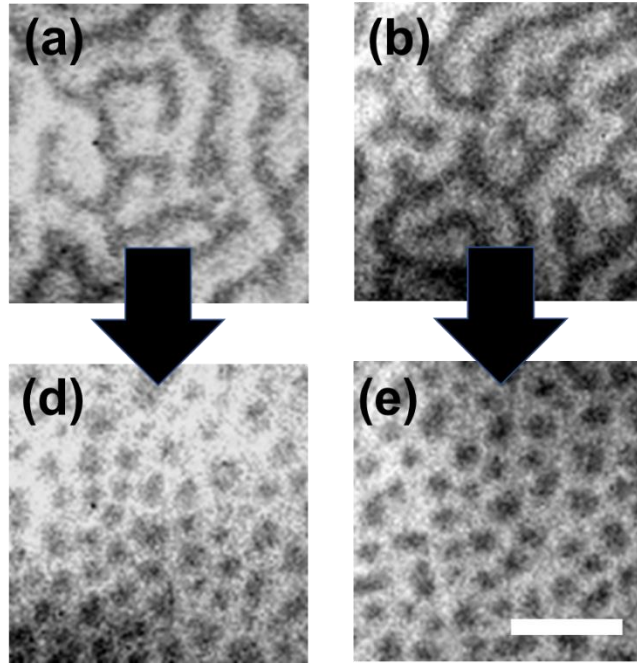
Supplemental Figure S3. (a) Out-of-plane and (b) in-plane vibrating sample magnetometry characterization of the room temperature magnetic properties of the Ta (2)/Pt (5)/[Co (0.7)/Spacer (0.4)/Ni (0.5)/Pt (0.7)]₂₀/Ta (5) (thicknesses in nm) samples. (c) Saturation magnetization (M_s) and effective perpendicular anisotropy energy density (K_{eff}) of the samples determined from (a) and (b).



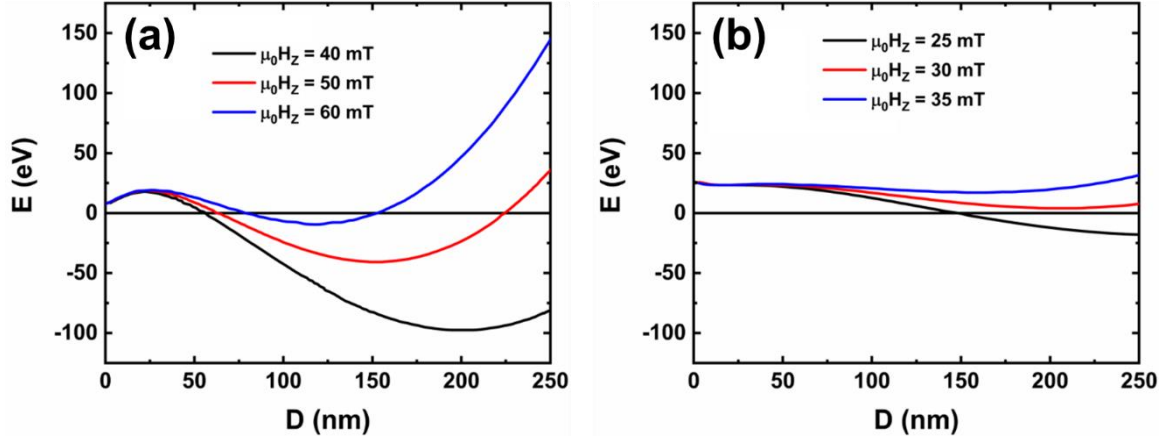
Supplemental Figure S4. MTXM images of the magnetic domain morphology as an out-of-plane magnetic field ($\mu_0 H_z$) was swept from zero towards positive saturation then back to zero in the Ta (2)/Pt (5)/[Co (0.7)/Tb (0.4)/Ni (0.5)/Pt (0.7)]₂₀/Ta (5) (thicknesses in nm) sample.



Supplemental Figure S5. MTXM images depicting the change in domain morphology of the Ta (2)/Pt (5)/[Co (0.7)/Tb (0.4)/Ni (0.5)/Pt (0.7)]₂₀/Ta (5) (thicknesses in nm) sample before (a) and after (b) a 200- μ s pulse of current density 2.4×10^9 A/m² was applied in an applied magnetic field of + 40 mT. The blue arrow indicates the electron flow j direction. (bar = 500 nm)



Supplemental Figure S6: MTXM images illustrating the effect of applying a $\tau = 50 \mu\text{s}$ -long current pulse with density $1.7 \times 10^{10} \text{ A/m}^2$ on the domain morphology of the (a) Ta (2)/Pt (5)/[Co (0.7)/ Ni (0.5)/Pt (0.7)]₂₀/Ta (5) sample and the (b) Ta (2)/Pt (5)/[Co (0.7)/ Ni (0.5)/Pt (0.7)]₂₀/Pt (5) (thicknesses in nm) samples in an applied magnetic field of +50 mT. (scale bar = 400 nm)



Supplemental Figure S7: The energy profile of isolated bubble domains at several perpendicular field strengths $\mu_0 H_z$ in proximity to the lowest $\mu_0 H_z$ necessary for skyrmion nucleation in the (a) Ta (2)/Pt (5)/[Co (0.7)/ Ni (0.5)/Pt (0.7)]₂₀/Ta (5) sample and the (b) Ta (2)/Pt (5)/[Co (0.7)/ Ni (0.5)/Pt (0.7)]₂₀/Pt (5) (thicknesses in nm) . The energy profile was calculated using the analytical treatment proposed in Ref 36. In calculating (a), sample properties of $M_S = 1000$ emu/cc, $K_u = 1.1 \times 10^7$ J/m³, DMI energy density of 0.6 mJ/m², and exchange stiffness $A = 10$ pJ/m were used. In calculating (b), sample properties of $M_S = 500$ emu/cc, $K_u = 1.7 \times 10^6$ J/m³, DMI energy density of 0.6 mJ/m², and exchange stiffness $A = 10$ pJ/m were used.

References

-
- ¹ S. Heinze, K. Bergmann, M. Menzel, J. Brede, A. Kubetzka, R. Wiesendanger, G. Bihlmayer, and S. Blugel, *Nature Phys.* **7**, 713 (2011).
- ² A. Fert, N. Reyren, V. Cros, *Nature Rev. Mat.* **2**, 17031 (2017).
- ³ S. Rohart, J. Miltat, and A. Thiaville, *Phys. Rev. B* **93**, 214412 (2016).
- ⁴ J. Grollier, D. Querlioz, K.Y. Camsari, K. Everschor-Sitte, S. Fukami, and M.D. Stiles, *Nature Electronics*, (2020).
- ⁵ S.A. Montoya, S. Couture, J.J. Chess, J.C.T. Lee, N. Kent, D. Henze, S.K. Sinha, M.-Y. Im, S.D. Kevan, P. Fischer, B.J. McMorran, V. Lomakin, S. Roy, and E.E. Fullerton, *Phys. Rev. B* **95**, 024415 (2017).
- ⁶ I. Dzyaloshinskii, *J. Phys. Chem. Solids* **4**, 241 (1958).
- ⁷ T. Moriya, *Phys. Rev.* **120**, 91 (1961).
- ⁸ O. Nakanishi, A. Yanase, A. Hasegawa, and M. Kataoka, *Solid State Commun.* **995** (1980).
- ⁹ S. Muhlbauer, B. Binz, F. Jonietz, C. Pfleiderer, A. Rosch, A. Neubauer, R. Goergii, and P. Boni, *Science* **323**, 915 (2009).
- ¹⁰ A. Fert, N. Reyren, and V. Cros, *Nat. Rev. Mat.* **2**, 17031 (2017).
- ¹¹ J. Sampaio, V. Cros, S. Rohart, A. Thiaville, and A. Fert, *Nat. Nanotech.* **8**, 839 (2013).
- ¹² A. Fert, V. Cros, and J. Sampaio, *Nature Nanotech.* **8**, 152 (2013).
- ¹³ M. Bode, M. Heide, K. von Bergmann, P. Ferriani, S. Heinze, G. Bihlmayer, A. Kubetzka, O. Pietzch, S. Blugel, and R. Wiesendanger, *Nature* **447**, 190 (2007).
- ¹⁴ H. Yang, O. Boulle, V. Cros, A. Fert, and M. Chshiev, *Sci. Rep.* **8**, 12356 (2018).
- ¹⁵ A. Soumyanarayanan, N. Reyren, A. Fert, and C. Panagopoulos, *Nature* **539**, 509 (2016).
- ¹⁶ C. Moreau-Luchaire, C. Moutafis, N. Reyren, J. Sampaio, C.A.F. Vaz, N. Van Horne, K. Bouzehouane, K. Garcia, C. Deranlot, P. Warnicke, P. Wohrluter, J.-M. George, M. Weigand, J. Raabe, V. Cros, and A. Fert, *Nature Nanotech.* **11**, 444 (2016).
- ¹⁷ S. Woo, K. Litzius, B. Kruger, M.-Y. Im, L. Caretta, K. Richter, M. Mann, A. Krone, R.M. Reeve, M. Weigand, P. Agrawal, I. Lemesch, M.-A. Mawass, P. Fischer, M. Klaui, and G.S.D. Beach, *Nature Mater.* **15**, 501 (2016).

-
- ¹⁸ R. Tolley, S.A. Montoya, and E.E. Fullerton, *Phys. Rev. Mat.* **2**, 044404 (2018).
- ¹⁹ W. Jiang, G. Chen, K. Liu, J. Zang, S.G.E. te Velthuis, and A. Hoffmann, *Phys. Rep.* **704**, 1 (2017).
- ²⁰ K. Everschor-Sitte, J. Masell, R.M. Reeve, and M. Klau, *J. Appl. Phys.* **124**, 240901 (2018).
- ²¹ I. Lemesh, K. Litzius, M. Bottcher, P. Bassirian, N. Kerber, D. Heinze, J. Zazvorka, F. Buttner, L. Caretta, M. Mann, M. Weigand, S. Finizio, J. Raabe, M.-Y. Im, H. Stoll, G. Schutz, B. Dupe, M. Klau, and G.S.D. Beach, *Adv. Mater.* **30**, 1805461 (2018).
- ²² W. Legrand, D. Maccariello, N. Reyren, K. Garcia, C. Moutafis, C. Moreau-Luchaire, S. Collin, K. Bouzehouane, V. Cros, and A. Fert, *Nano Lett.* **17**, 2703 (2017).
- ²³ F. Buttner, M.A. Mawass, J. Bauer, E. Rosenberg, L. Caretta, C.O. Avci, J. Grafe, S. Finizio, C.A.F. Vaz, N. Novakovic, M. Weigand, K. Litzius, J. Forster, N. Trager, F. Gross, D. Suzuki, M. Huang, J. Bartell, F. Kronast, J. Raabe, G. Schutz, C.A. Ross, and G.S.D. Beach, *Phys. Rev. Mat.* **4**, 011401(R) (2020).
- ²⁴ Z. Wang, M. Guo, H.-A. Zhou, L. Zhao, T. Xu, R. Tomasello, H. Bai, Y. Dong, S.G. Je, W. Chao, H.-S. Han, S. Lee, K.-S. Lee, Y. Yao, W. Han, C. Song, H. Wu, M. Carpentieri, G. Finocchio, M.-Y. Im, S.-Z. Lin, and W. Jiang, *arXiv:2005.0744*
- ²⁵ W. Koshibae and N. Nagaosa, *Nature Comm.* **5**, 5148 (2014).
- ²⁶ P. Jadaun, L.F. Register, and S.K. Banerjee, **arXiv:1903.09345**
- ²⁷ S. Andrieu, T. Hauet, M. Gottwald, A. Rajanikanth, L. Calmels, A.M. Bataille, F. Montaigne, S. Mangin, E. Otero, P. Ohresser, P. Le Fevre, F. Bertran, A. Resta, A. Vlad, A. Coati, and Y. Garreau, *Phys. Rev. Mat.* **2**, 064410 (2018).
- ²⁸ M. Gottwald, S. Andrieu, F. Gimbert, E. Shipton, L. Calmels, C. Magen, E. Snoeck, M. Liberati, T. Hauet, E. Arenholz, S. Mangin, and E.E. Fullerton, *Phys. Rev. B* **86**, 014425 (2012).
- ²⁹ M. Li, D. Lau, M. De Graef, and V. Sokalski, *Phys. Rev. Mat.* **3**, 064409 (2019).
- ³⁰ A. Hrabec, J. Sampaio, M. Belmeguenai, I. Gross, R. Weil, S.M. Cherif, A. Stashkevich, V. Jacques, A. Thiaville, and S. Rohart, *Nature Comm.* **8**, 15765 (2017).
- ³¹ See Supplemental Material for images of the field-dependent morphology in continuous Co/Ni/Pt-based films, more detailed images of the effects of varying current pulses, static magnetic characterization, the effect of changing the capping layer composition, and analytic modeling of the size and stability in Co/Ni/Pt-based films.

-
- ³² K. Zeissler, M. Mruczkiewicz, S. Finizio, J. Raabe, P.M. Shepley, A.V. Sadovnikov, S.A. Nikitov, K. Fallon, S. McFadzean, S. McVitie, T.A. Moore, G. Burnell, and C.H. Marrows, *Sci. Rep.* **7**, 15125 (2017).
- ³³ R. Juge, S.G. Je, D. de Souza Chaves, S. Pizzini, L.D. Buda-Prejbeanu, L. Aballe, M. Foerster, A. Locatelli, T. Onur Montes, A. Sala, F. Maccherozzi, S.S. Dhesi, S. Auffret, E. Gautier, G. Gaudin, J. Vogel, and O. Boulle, *J. Magn. Magn. Mater.* **455**, 3 (2018).
- ³⁴ W. Akhtar, A. Hrabec, S. Chouaieb, A. Haykal, I. Gross, M. Belmeguenai, M.S. Gabor, B. Shields, P. Maletinsky, A. Thiaville, S. Rohart, and V. Jacques, *Phys. Rev. Appl.* **11**, 034066 (2019).
- ³⁵ M. Herve, B. Dupe, R. Lopes, M. Bottcher, M.D. Martins, T. Balashov, L. Gerhard, J. Sinova, and W. Wulfskel, *Nature Comm.* **9**, 1015 (2018).
- ³⁶ F. Buttner, I. Lemesh, and G.S.D. Beach, *Sci. Rep.* **8**, 4464 (2018).
- ³⁷ M.A. Basha, C.L. Prajapat, M. Gupta, H. Bhatt, Y. Kumar, S.K. Ghosh, V. Karki, S. Basu, and S. Singh, *Phys. Chem. Chem. Phys.* **20**, 21580 (2018).
- ³⁸ R. E. Camley and D. R. Tilley, *Phys. Rev. B* **37**, 3413 (1988).
- ³⁹ M.R. Hossu and A.R. Koymen, *J. Appl. Phys.* **99**, 08C704 (2006).
- ⁴⁰ Z.S. Shan and D.J. Sellmyer, *Phys. Rev. B* **42**, 10433 (1990).
- ⁴¹ C. Kittel, *Phys. Rev.* **70**, 965 (1946).
- ⁴² L. Liu, C.-F. Pai, Y. Li, H.W. Tseng, D.C. Ralph, and R.A. Buhrman, *Science* **336**, 555 (2012).
- ⁴³ M. Althammer, S. Meyer, H. Nakayama, M. Schreier, S. Altmannshofer, M. Weiler, H. Huebl, S. Geprags, M. Opel, R. Gross, D. Meier, C. Klewe, T. Kuschel, J.-M. Schmalhorst, G. Reiss, L. Shen, A. Gupta, Y.-T. Chen, G.E.W. Bauer, E. Saitoh, and S.T.B. Goennenwein, *Phys. Rev. B* **87**, 224401 (2013).
- ⁴⁴ D. Li, S. Chen, Y. Zuo, J. Yun, B. Cui, K. Wu, X. Guo, D. Yang, J. Wang, and L. Xi, *Sci. Rep.* **8**, 12959 (2018).
- ⁴⁵ W. Legrand, J.-Y. Chauleau, D. Maccariello, N. Reyren, S. Collin, K. Bouzehouane, N. Jaouen, V. Cros, and A. Fert, *Science Advances* **4**, 0415 (2018).
- ⁴⁶ S.-G. Je, D.H. Kim, S.C. Yoo, B.C. Min, K.J. Lee, and S.B. Choe, *Phys. Rev. B* **88**, 214401 (2013).

⁴⁷ P. Fischer, D-H. Kim, B.L. Mesler, W. Chao, A.E. Sakdinawat, and E.H. Anderson, *Surf. Sci.* **601**, 4680 (2007).